



WISEA J083011.95+283716.0: A Missing Link Planetary-mass Object

Daniella C. Bardalez Gagliuffi¹, Jacqueline K. Faherty¹, Adam C. Schneider², Aaron Meisner³, Dan Caselden⁴, Guillaume Colin⁴, Sam Goodman⁴, J. Davy Kirkpatrick⁵, Marc Kuchner⁶, Jonathan Gagné⁷, Sarah E. Logsdon⁸, Adam J. Burgasser⁹, Katelyn Allers¹⁰, John Debes¹¹, John Wisniewski¹², Austin Rothermich¹³, Nikolaj Stevnbak Andersen¹⁴, Melina Thévenot⁴, and Jim Walla⁴

Backyard Worlds: Planet 9 Collaboration

¹ American Museum of Natural History, 200 Central Park West, New York, NY 10024, USA; dbardalezgagliuffi@amnh.org

² School of Earth and Space Exploration, Arizona State University, 781 Terrace Mall, Tempe, AZ 85287, USA

³ NSF's National Optical-Infrared Astronomy Research Laboratory, 950 N Cherry Avenue, Tucson, AZ 85719, USA

⁴ Backyard Worlds: Planet 9

⁵ IPAC, Mail Code 100-22, Caltech, 1200 E. California Boulevard, Pasadena, CA 91125, USA

⁶ NASA Goddard Space Flight Center, Exoplanets and Stellar Astrophysics Laboratory, Code 667, Greenbelt, MD 20771, USA

⁷ Institut de Recherche sur les Exoplanètes, Université de Montréal, Pavillon Roger-Gaudry, P.O. Box 6128 Centre-Ville STN, Montreal QC H3C 3J7, Canada

⁸ National Optical Astronomy Observatory, 950 N Cherry Avenue, Tucson, AZ 85719, USA

⁹ Center for Astrophysics and Space Sciences, University of California, San Diego, 9500 Gilman Drive, Mail Code 0424, La Jolla, CA 92093, USA

¹⁰ Physics and Astronomy Department, Bucknell University, 701 Moore Avenue, Lewisburg, PA 17837, USA

¹¹ Space Telescope Science Institute, Baltimore, MD 21218, USA

¹² Homer L. Dodge Department of Physics and Astronomy, University of Oklahoma, 440 West Brooks Street, Norman, OK 73019, USA

¹³ Physics Department, University Of Central Florida, 4000 Central Florida Boulevard, Building 12, 310, Orlando, FL 32816, USA

¹⁴ Kolding Hospital, Department of Cardiology, Sygehus Lillebalt 24, 6000 Kolding, Denmark
Received 2020 February 4; revised 2020 April 23; accepted 2020 April 25; published 2020 June 5

Abstract

We present the discovery of WISEA J083011.95+283716.0, the first Y-dwarf candidate identified through the “Backyard Worlds: Planet 9” citizen science project. We identified this object as a red, fast-moving source with a faint *W2* detection in multiepoch ALLWISE and unWISE images. We have characterized this object with Spitzer and Hubble Space Telescope’s (HST) follow-up imaging. With mid-infrared detections in Spitzer’s *ch1* and *ch2* bands and flux upper limits in HST *F105W* and *F125W* filters, we find that this object is both very faint and has extremely red colors ($ch1 - ch2 = 3.25 \pm 0.23$ mag, $F125W - ch2 \geq 9.36$ mag), consistent with a $T_{\text{eff}} \sim 300$ K source, as estimated from the known Y-dwarf population. A preliminary parallax provides a distance of $11.1_{-1.5}^{+2.0}$ pc, leading to a slightly warmer temperature of ~ 350 K. The extreme faintness and red HST and Spitzer colors of this object suggest that it may be a link between the broader Y-dwarf population and the coldest known brown dwarf WISE J0855–0714, and may highlight our limited knowledge of the true spread of Y-dwarf colors. We also present four additional “Backyard Worlds: Planet 9” late-T brown dwarf discoveries within 30 pc.

Unified Astronomy Thesaurus concepts: [Brown dwarfs \(185\)](#); [Y dwarfs \(1827\)](#); [HST photometry \(756\)](#); [Hubble Space Telescope \(761\)](#); [Near infrared astronomy \(1093\)](#); [Infrared telescopes \(794\)](#); [Infrared astronomy \(786\)](#); [Infrared photometry \(792\)](#); [Infrared sources \(793\)](#); [Space telescopes \(1547\)](#); [Proper motions \(1295\)](#); [Parallax \(1197\)](#)

1. Introduction

With temperatures below ~ 500 K, Y dwarfs are the coldest products of star formation (Cushing et al. 2011), and are well within the temperature and mass range of old giant planets. Detecting Y dwarfs was a key goal of the Wide Field Infrared Survey Explorer (WISE; Wright et al. 2010), with a mid-infrared filter designed specifically to cover the flux peak of these objects ($\lambda_{W2} = 4.6 \mu\text{m}$). Several discoveries from this mission have reshaped the landscape of the solar neighborhood: WISE J085510.83–071442.5 (hereafter WISE J0855–0714), the fourth-closest system to the Sun (2.31 ± 0.08 pc; Luhman & Esplin 2014) and the coldest known brown dwarf to date at ~ 250 K (Luhman 2014); WISE J104915.57–531906.1, the closest brown dwarf binary to the Sun, also at 2 pc (2.02 ± 0.019 pc; Boffin et al. 2014); and WISE J072003.20–084651.2AB, an M9+T5 dwarf spectral binary system at 6 pc, which traversed the Oort cloud about 70,000 years ago at only 0.25 pc (Scholz 2014; Burgasser et al. 2015; Mamajek et al. 2015), and whose T-dwarf component is more

massive than predicted from evolutionary models (Dupuy et al. 2019). More recent discoveries have capitalized on multiepoch WISE photometry to reach fainter objects than previous detection thresholds allowed, like the ~ 270 – 360 K Y dwarf CWISEP J193518.59–154620.3 (hereafter CWISEP J1935–1546; Marocco et al. 2019), and the ~ 310 – 360 K CWISEP J144606.62–231717.8 (hereafter CWISEP J1446–2317; Marocco et al. 2020; Meisner et al. 2020). Nevertheless, the currently known Y-dwarf population remains small, totaling only 28 objects (Cushing et al. 2011; Luhman et al. 2011; Kirkpatrick et al. 2012, 2013; Liu et al. 2012; Tinney et al. 2012, 2014, 2018; Luhman 2014; Pinfield et al. 2014; Dupuy et al. 2015; Schneider et al. 2015; Martin et al. 2018; Marocco et al. 2019, 2020).

Even with this small sample, Kirkpatrick et al. (2019) placed initial constraints on the field luminosity and mass functions of brown dwarfs at cold temperatures. This study found that a single power-law mass function extending down to $5 M_{\text{Jup}}$ provided a good fit to the number density of nearby brown dwarfs. However, sampling is particularly sparse at the lowest

temperatures, with WISE J0855–0714 being the only object in the 150–300 K temperature range. A larger volume-limited sample of Y dwarfs is needed to improve the statistical measurement of the luminosity function at these temperatures to constrain the low-mass limit of star formation (Burgasser 2004). Similarly, a statistical sample of Y dwarfs is needed to characterize the composition, structure, and dynamics of low-temperature atmospheres (e.g., Faherty et al. 2014; Skemer et al. 2016), and to possibly identify spectroscopic markers of different formation pathways between brown dwarfs and giant planets (e.g., Morley et al. 2019).

Y dwarfs have complex atmospheres that resemble those of giant planets, with deep absorption features from CH₄, H₂O, and possibly NH₃ (Burrows et al. 2003; Burgasser et al. 2012), and ice water clouds (Morley et al. 2014a). As they are not outshined by a host star, these objects generally are ideal proxies to conduct exoplanet atmospheric characterization studies. However, due to their intrinsic faintness, objects with spectral types later than Y1 either do not have spectroscopic measurements or have poor signal-to-noise data that prevent the clear identification of molecular absorption lines and bands. For example, phosphine, salt, and sulfide clouds, similar to those found in the atmospheres of Jupiter (Visscher et al. 2006), were predicted to affect the mid-infrared spectra of Y dwarfs (Morley et al. 2012). However, phosphine was not identified in the M-band spectrum of the 250 K WISE J0855–0714 (Skemer et al. 2016; Morley et al. 2018), nor were salt or sulfide clouds, even though their presence is favored by atmospheric retrieval models (Zalesky et al. 2019). Y dwarfs are prime targets for medium-resolution spectroscopy with the James Webb Space Telescope (JWST) to solidly determine their atmospheric composition.

Despite the growth in the known population of cold brown dwarfs, there remain two brightness and temperature gaps between the majority of the known Y dwarfs, WISE J0855–0714, and gas giants like Jupiter (~125 K; Hanel et al. 1981). To look for the faintest objects missed in previous searches, the “Backyard Worlds: Planet 9” citizen science project (BYW:P9) is harnessing the power of visual inspection of multiepoch and multiwavelength imaging. The goal of this project is to identify the faintest, coldest, and fastest-moving sources in the solar neighborhood through time-resolved WISE coadded animations (unWISE; Meisner et al. 2017a, 2017b, 2018a). BYW:P9 was launched in 2017 February (Kuchner et al. 2017) as part of the Zooniverse ecosystem. Since then, over 150,000 users around the world have participated in the visual identification and classification of new brown dwarf candidates through the Backyard Worlds interface.¹⁵ Prior discoveries include the lowest binding energy ultracool binary in the field (Faherty et al. 2020), a white dwarf with infrared excess (Debes et al. 2019), and two T-type subdwarfs (Schneider et al. 2020).

In this paper, we present the discovery and space-based follow-up observations of five new low-temperature brown dwarfs identified by “Backyard Worlds: Planet 9” citizen scientists, including one Y dwarf. Section 2 describes the five targets of our sample. Section 3 describes the observations with the Hubble and Spitzer space telescopes and our photometric measurements. Section 4 shows our parallax calculation and estimated quantities based on our infrared color analysis. Section 5 discusses the implications of our discoveries for our

understanding of the T/Y transition, the census of the solar neighborhood, and brown dwarf formation at the lowest masses.

2. Target Sample

The WISE observing strategy consists of scanning the entire sky every six months, with over 12 exposures per visit. Coadding exposures from the full cryogenic WISE (Wright et al. 2010), NEOWISE (Mainzer et al. 2011), and NEOWISE Reactivation missions (NEOWISER; Mainzer et al. 2014), led to the generation of full-depth, “unWISE” images in W1 and W2 filters (Meisner et al. 2017b, 2018a). These images reach ~1.3 mag fainter than single exposures, and are used for the identification of faint, fast-moving sources through BYW:P9.

Our sample contains five sources identified by citizen scientists from the BYW:P9 collaboration due to their red color in W1–W2 and fast proper motion in the 5.5 yr baseline of unWISE images (Meisner et al. 2018a, 2018b). None of these objects are detected in the near-infrared Two Micron All Sky Survey (Skrutskie et al. 2006), the UKIRT Hemisphere Survey (Dye et al. 2018), or the VISTA Hemisphere Survey (McMahon et al. 2013). In the mid-infrared, our five sources have only flux upper limit AllWISE photometry in W1 and detections with large uncertainties in W2, leading to uncertain W1–W2 colors that nevertheless indicate extremely faint and red objects.

The precision and accuracy of the photometry and proper motions of these objects are significantly improved in the CatWISE Preliminary catalog (Eisenhardt et al. 2020) relative to AllWISE. CatWISE is a new catalog resulting from running the AllWISE software on unWISE images using NEOWISE epochs, yielding 10X better per-coordinate proper motion uncertainty at W1 ~1.5 mag, and is 3 mag more sensitive than AllWISE at 100 mas yr⁻¹. As AllWISE proper motions are generally unreliable at W2 ≥ 13.5 mag (Kirkpatrick et al. 2016), and have been superseded by CatWISE, we present only CatWISE photometry and proper motions in Table 1 and use these measurements in the analysis that follows.

Using multiepoch unWISE data (Meisner et al. 2018a), we measured proper motions for each source and placed them in a reduced proper motion diagram, traditionally used to distinguish faint main-sequence stars from subdwarfs and cool, white dwarfs if parallaxes are absent, acting as a proxy for absolute magnitude (Luyten 1922). For our BYW:P9 Hubble Space Telescope (HST) follow-up, we prioritized five sources that overlap with the known Y-dwarf population (see Figure 1). These sources were also observed as part of our Spitzer follow-up program. In the next sections, we characterize these sources with both sets of photometry.

3. Observations

3.1. WFC3/HST Photometry

Our targets were observed between UT 2018 August 11 and UT 2019 February 16 in 5 HST orbits under GO program 15468 (PI: Faherty). All five targets were observed with both F105W ($\lambda_c = 1055.2$ nm) and F125W ($\lambda_c = 1248.6$ nm) filters on the Wide Field Camera 3 (WFC3; MacKenty et al. 2008), which roughly coincide with the Y and J near-infrared bands. All of the observations were done in MULTIACUUM mode with four dither positions per source per filter in a 123'' × 135'' field of view. Total exposure times are listed in Table 2. Scheduled observations of WISEA J1516+7217 on UT 2018

¹⁵ www.BackyardWorlds.org

Table 1
CatWISE Photometry and Proper Motions

Source	CatWISE Designation	W1 (mag)	W2 (mag)	W1 – W2 (mag)	μ_α (mas yr ⁻¹)	μ_δ (mas yr ⁻¹)	μ_{total} (mas yr ⁻¹)
WISEA J001449.96+795116.1	CWISEP J001450.72+795116.0	18.72 ± 0.28	16.00 ± 0.06	2.72 ± 0.28	531.2 ± 89.2	-20.7 ± 77.8	531.6 ± 89.2
WISEA J083011.95+283716.0 ^a	CWISEP J083011.94+283716.2	≥18.0	16.639 ± 0.188	≥1.33	-730.40 ± 290.7	-1161.20 ± 367.0	1371.43 ± 468.18
	CWISEP J083011.94+283706.1	≥18.9	16.052 ± 0.092	≥2.9	54.3 ± 153.5	-314.3 ± 154.1	319.0 ± 154.1
WISEA J083019.97-632305.4	CWISEP J083019.95-632304.2	18.12 ± 0.10	15.87 ± 0.04	2.25 ± 0.10	-81.7 ± 65.4	375.0 ± 64.7	383.8 ± 64.7
WISEA J151620.39+721745.4	CWISEP J151620.00+721747.9	18.91 ± 0.17	16.13 ± 0.05	2.79 ± 0.18	-562.2 ± 89.9	560.8 ± 78.9	794.1 ± 84.5
WISEA J152529.09+605356.5	CWISEP J152528.90+605359.0	≥19.7	15.99 ± 0.05	≥3.7	-394.2 ± 85.1	763.7 ± 85.6	859.4 ± 85.5

Notes. Object names are from AllWISE, magnitudes and proper motions are updated from CatWISE. For CatWISE, we report photometry from the `w1mpro_pm` and `w2mpro_pm` keywords and their associated uncertainties.

^a Two CatWISE entries are found when searching for the AllWISE source WISEA J083011.95+283716.0. This object has such a high proper motion that the CatWISE pipeline confused it as two sources. The photometry and proper motion reported in CatWISE for this object are unreliable. Our Spitzer photometry (Table 3) and astrometry (Table 4) supersede the values reported in this table for this object.

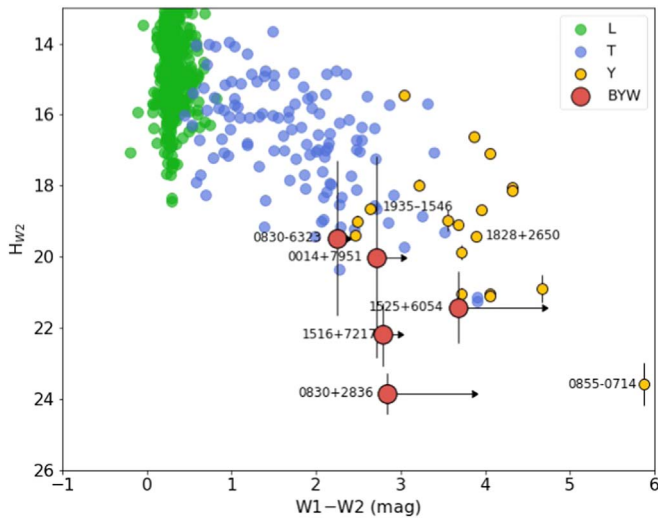


Figure 1. Reduced proper motion diagram in W2 band from AllWISE. All five objects in our sample are flux upper limits in W1 from AllWISE. Background M, L, and T dwarfs come from Faherty et al. (2009, 2012). Y dwarfs are compiled from Kirkpatrick et al. (2019).

November 5 were taken on gyros only, after failing to acquire a guide star, but these were rescheduled and successfully acquired on UT 2019 February 16. The individual exposures per filter were combined, cleaned of cosmic rays, and registered to the World Coordinate System with the `tweakreg` and `astrodrizzle` routines available in the `AstroDrizzle` software (Gonzaga et al. 2012).

Photometry was calculated on the drizzled images using a custom function¹⁶ built with routines from the `photutils` Python package. Centroids were determined using the `DAOStarFinder` Python routine based on the `DAOFIND` algorithm (Stetson 1987). This algorithm uses a 2D Gaussian kernel to search for local maxima with a peak amplitude greater than a given threshold. We chose a full-width half maximum of three pixels and a threshold of five times the median absolute deviation in a 50-by-50 pixel cut-out of the science images centered on the targets. This method yielded more accurate results than other 1D and 2D Gaussian fitting techniques (e.g., `photutils.centroids`).

WFC3 pixels become correlated after the drizzling process, so rather than calculating the background flux with an annulus around the target, we followed the prescription of Schneider et al. (2015). The contribution of the sky background was estimated by randomly placing 10,000 apertures on the image, and calculating aperture photometry on them. The radius for these apertures was $0''.4$ in flux units of $e^- s^{-1}$, thus matching the one used for aperture photometry on the sources, as defined in the *WFC3* Data Handbook (Gennaro 2018). The array of background count values was sigma clipped to 3σ to avoid contribution from apertures containing stars or anomalous negative-count pixels. The median and standard deviation of the background are used as the value and uncertainty in the sky contribution.

Aperture photometry on the stellar sources was calculated using the same radius of $0''.4$. The final source flux was obtained by subtracting the background flux from the aperture flux, as both aperture areas were the same. Magnitudes in the Vega system were directly calculated from the fluxes using

zero-points of 25.4523 mag and 25.1439 mag for the *F105W* and *F125W* filters, respectively, as defined by the HST/WFC3 data handbook (Gennaro 2018). Uncertainties on the stellar flux were estimated following the DAOPHOT photometry error method (Stetson 1987) and include Poisson error contributions from stellar and background counts and read error from the detector:

$$\sigma_{\text{tot}} = \frac{\sqrt{\frac{F \Delta t_{\text{exp}}}{g_{\text{eff}}} + A(\sigma_{\text{bkg}} \Delta t_{\text{exp}})^2 + A^2 \frac{(\sigma_{\text{bkg}} \Delta t_{\text{exp}})^2}{N_{\text{sky}}}}}{\Delta t_{\text{exp}}}, \quad (1)$$

where F is the raw aperture flux (including both stellar and background contributions), Δt_{exp} is the exposure time, g_{eff} is the effective gain, A is the aperture area, σ_{bkg} is the standard deviation of the background in $e^- s^{-1}$, and N_{sky} is the number of sky pixels used to estimate the background. As the WFC3 images come in units of $e^- s^{-1}$, the effective gain can be estimated as the total exposure time,¹⁷ as extracted from the FITS headers. For a total uncertainty per pixel per second, this equation can be reduced to

$$\sigma_{\text{tot}} = \sqrt{\frac{F}{\Delta t_{\text{exp}}} + 2\sigma_{\text{bkg}}^2}. \quad (2)$$

For the case of WISEA J0830+2837, which is undetected in both HST filters, we estimate a 3σ upper limit on flux from the standard deviation of the flux from the 10,000 background apertures.

The HST images of WISEA J0014+7951 reveal a nearby fainter source $1''.2$ away at a position angle of $231^\circ.52$ east of north. We measured *F105W* and *F125W* magnitudes of 24.07 ± 0.265 mag and 23.59 ± 0.271 mag, respectively, leading to an HST color of 0.48 ± 0.38 mag. This source is ~ 3 mag fainter than our WISEA J0014+7951 target in both bands (*F105W* = 20.924 ± 0.015 mag, *F125W* = 19.993 ± 0.008 mag), and its HST color is roughly half a magnitude bluer than the HST color of WISEA J0014+7951 (*F105W*–*F125W* = 0.931 ± 0.017 mag, see Table 3). We hypothesize that if this object were a true companion to the T8 WISEA J0014+7951, by definition it would be cooler, later-type, and hence redder (see Schneider et al. 2015, 2016; Kirkpatrick et al. 2019). However, given the bluer HST color, it is unlikely that these two objects are associated. Unfortunately, these two sources are blended in our Spitzer images, so we are unable to measure a second color to better characterize this object.

3.2. Spitzer Photometry

In addition to the HST photometry, we also obtained Spitzer photometry for these five targets, as part of program ID 14076 (PI: Faherty). The observations followed a 16-point spiral dither pattern with 30 s exposures per frame. Data were acquired with both *ch1* and *ch2* filters. Readout was done in full array mode.

Aperture photometry was measured using the Spitzer MOsaicker and Point SExtractor with point-source extraction package (MOPEX/APEX; Makovoz & Marleau 2005), and can be found in Table 2. Specifically, we used the corrected basic calibrated data frames to build custom mosaics from

¹⁶ Found at <https://github.com/daniellabardalezgagliuffi/HSTphotometry>.

¹⁷ See https://photutils.readthedocs.io/en/stable/api/photutils.utils.calc_total_error.html for more details.

Table 2
Summary of HST and Spitzer Observations

Source	R.A.	Decl.	Obs. Date	Total Exp. Time (s)	Filter
HST					
WISEA J0014+7951	00 15 01.32	+79 51 08.08	2018 Aug 11	1412	F105W
				1412	F125W
WISEA J0830+2837	08 30 11.89	+28 36 58.23	2018 Sep 29	1212	F105W
				1312	F125W
WISEA J0830–6323	08 30 19.95	–63 22 59.97	2018 Aug 29	1312	F105W
				1412	F125W
WISEA J1516+7217	15 16 19.43	+72 17 53.81	2019 Feb 16	1412	F105W
				1412	F125W
WISEA J1525+6053	15 25 28.65	+60 54 03.32	2018 Nov 5	1312	F105W
				1412	F125W
Spitzer					
WISEA J0014+7951	00 14 49.96	+79 51 16.2	2018 Dec 16	378	ch1
				378	ch2
WISEA J0830+2837	08 30 11.96	+28 37 16.0	2019 Feb 21	378	ch1
				378	ch2
WISEA J0830–6323	08 30 19.98	–63 23 05.5	2018 Aug 14	378	ch1
				378	ch2
WISEA J1516+7217	15 16 20.40	+72 17 45.5	2019 Feb 11	378	ch1
				378	ch2
WISEA J1525+6053	15 25 29.10	+60 53 56.6	2018 Oct 21	378	ch1
				378	ch2

which the fluxes were measured using a 4 pixel aperture. These raw fluxes were converted to magnitudes by applying an aperture correction and comparing with the published *ch1* and *ch2* flux zero-points, as described in Section 5.1 of Kirkpatrick et al. (2019). Figure 2 shows the finder charts for this object for the unWISE, HST, and Spitzer epochs.

4. Analysis

4.1. Preliminary Parallax of WISEA J0830+2837

Spitzer *ch2* imaging of WISEA J0830+2837 was obtained in 2019 February via program 14076 (PI: Faherty) and in 2019 July–August via program 14224 (PI: Kirkpatrick). Astrometry was measured from the Spitzer images using the methodology described in Section 5.2 of Kirkpatrick et al. (2019) with a couple of exceptions. First, we used reregistration stars sampling down to smaller signal-to-noise ratio (S/N) values ($S/N = 30$) in order to have a larger selection of objects per frame that match Gaia DR2 sources with full astrometric solutions. Second, we used the full astrometric solutions of these reregistration stars to place each frame on an absolute astrometric grid: that is, we move each Gaia source to its expected position at that epoch and reregister the frame to that epoch-specific reference. This enables us to measure an absolute parallax, obviating the need to apply an ad hoc relative-to-absolute adjustment later.

After the original photometric follow-up in program 14076, we had only one additional visibility window available to us in program 14224 with which to measure astrometry for this object, because the Spitzer mission ceased operations on 2020 January 30. The data from programs 14,076 and 14,224 sample opposite sides of the parallactic ellipse, since they are separated by ~ 6 months, but at least one other epoch of data is needed to disentangle proper motion from parallax. We therefore used source detections from the unWISE epochal coadds (Lang 2014)

in a region around WISE 0830+2837, re-registered their positions to the Gaia DR2 reference frame, and used the resulting re-registered unWISE astrometry to provide eleven additional epochs spanning 2010 April to 2018 October. (See Meisner et al. 2020 for more details on the process.) These unWISE data were then associated with the appropriate XYZ position of the Earth at the mean time of each of the eleven unWISE epochs in the ICRS reference frame. A combined proper motion + parallax solution was fit using the methodology outlined in Section 5.2.3 of Kirkpatrick et al. (2019).

Our resulting solution is given in Table 4 and illustrated in Figure 3. The parallactic solution should be considered preliminary and somewhat fragile because there is a single high-quality data point anchoring one side of the parallactic ellipse. This is further demonstrated by the large parallactic error of $\sim 15\%$.

We find that the parallax is 90.6 ± 13.7 mas, implying a distance of $11.1_{-1.5}^{+2.0}$ pc. This parallax indicates an absolute magnitude in *ch2* of 15.61 ± 0.05 mag, which leads to a temperature range of 281–427 K following the Kirkpatrick et al. (2019) empirical relations.

4.2. Near and Mid-infrared Colors and Estimated Quantities

Equipped with HST and Spitzer photometry, we can characterize these objects in the context of other T and Y dwarfs. We have summarized the physical properties from the sample in Table 5. We have gathered colors from 14 late-T and Y dwarfs with HST and Spitzer photometry in the literature (Schneider et al. 2015, 2016) and used these as a comparison sample. Figure 4 shows our five targets in *ch1* – *ch2* versus *F125W* – *ch2* color–color space. Based on the colors of the comparison sample, it appears that all the objects in our sample, except for WISEA J0830+2837, are late-T dwarfs. WISEA J0830+2837 appears to be an early Y dwarf (Table 3, and Figure 5).

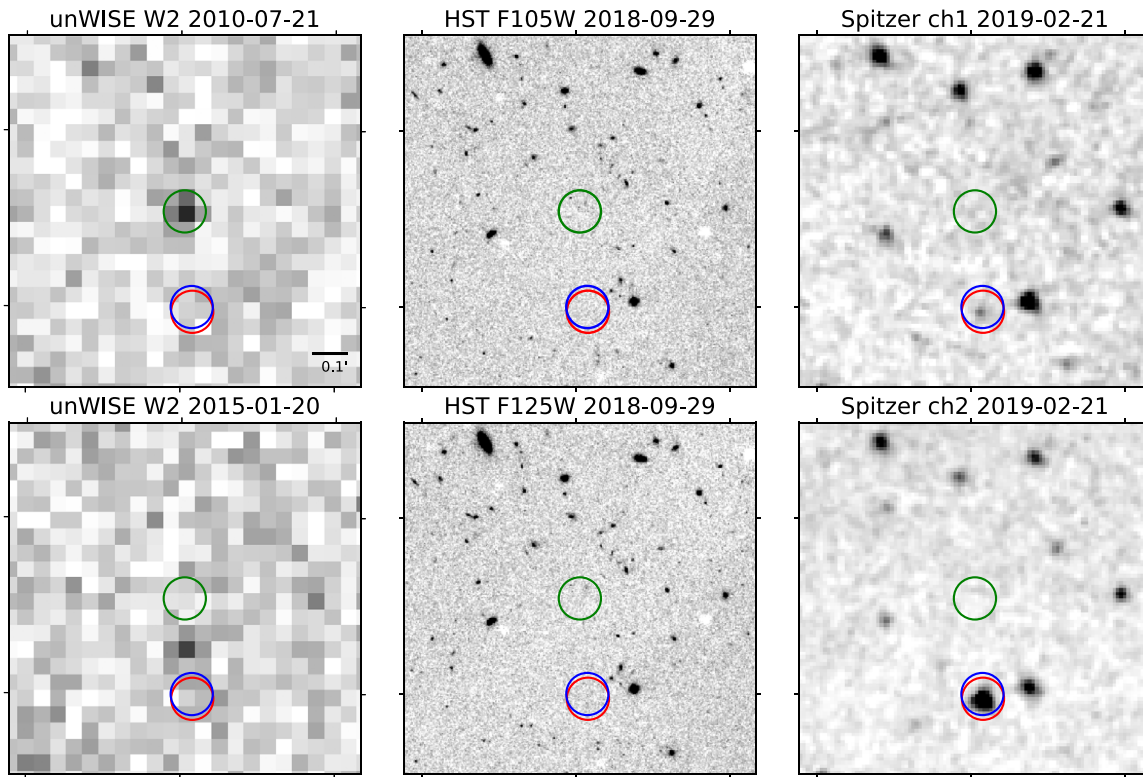


Figure 2. Finder charts for WISEA J0830+2837 of $1'$ per side. All frames are centered on the source at the first unWISE epoch (top left) and aligned north up, east to the left. unWISE positions are shown in green, HST positions in blue, and Spitzer positions in red. Significant proper motion can be seen between the two epochs of unWISE images. For HST images, we estimated the location of the source based on the Spitzer location and proper motion. The source is significantly brighter in Spitzer $ch2$ compared with $ch1$, and not detected in the NIR HST filters, signaling an extremely cold object.

Following the Kirkpatrick et al. (2019) relations for absolute magnitude in $ch2$, we estimate distances of 23–28 pc for our T-dwarf candidates, and $8.7_{-1.9}^{+2.3}$ pc for WISEA J0830+2837, with Monte Carlo uncertainties at the 16th and 84th percentiles. This photometric distance is consistent with the parallax measurement within uncertainties. However, it is worth noting that the empirical relations rely on one data point beyond $ch1 - ch2 \sim 3.5$ mag or $M_{ch2} \sim 16$ mag, corresponding to WISE J0855–0714, hence making any color-based estimation extremely tentative.

From every standpoint, WISEA J0830+2837 is an outlier in our sample. This object is undetected in both HST $F105W$ and $F125W$ filters, thus we only have flux upper limits. In Spitzer colors, however, this source is detected with moderately large error bars. It is the faintest object in $ch1$ in our sample, and the second brightest in $ch2$. The Spitzer $ch1 - ch2$ colors for our five targets are in the 1.8–2.1 mag range with the exception of WISEA J0830+2837, which has the reddest $ch1 - ch2$ color of the sample ($ch1 - ch2 = 3.25 \pm 0.23$ mag). Its color is comparable to CWISEP J1935–1546 ($ch1 - ch2 = 2.984 \pm 0.034$ mag, Meisner et al. 2020), and within 1σ of the Spitzer color of WISE J0855–0714 ($\Delta ch1 - ch2 = 0.3 \pm 0.2$ mag). Additionally, from the Spitzer colors of WISEA J0830+2837, we can estimate an effective temperature of ~ 300 K for this object (Kirkpatrick et al. 2019), also analogous to CWISEP J1935–1546 with a temperature (270–360 K). These two objects appear to be “missing links” filling the gap between most known Y dwarfs and WISE J0855–0714.

Based on parallax and proper motion of WISEA J0830+2837 with Spitzer, we can estimate a tangential velocity of $V_{\text{tan}} = 107.9 \pm 16.67$ km s $^{-1}$, which is significantly higher

than the median V_{tan} and velocity dispersion (σ_{tan}) for the nearby T-dwarf population (31 km s $^{-1}$ and 20 km s $^{-1}$, respectively; Faherty et al. 2012). The V_{tan} of this object is also higher than that of comparable objects, such as the Y dwarf WISE J163940.83?684738.6 (Tinney et al. 2012), with a $V_{\text{tan}} = 73 \pm 8$ km s $^{-1}$. The high V_{tan} of WISEA J0830+2837 suggests a kinematically old age. Assuming an age between 1 and 10 Gyr for this object, we estimate a mass of 4–13 M_{Jup} using the Baraffe et al. (2015) evolutionary models. Therefore, WISEA J0830+2837 is likely a planetary-mass object.

5. Discussion

5.1. The Low-mass End of the Substellar IMF

As shown in Figure 6, WISEA J0830+2837 is one of the faintest and reddest objects in the Y-dwarf population. Similar in brightness and Spitzer color are CWISEP J1935–1546 (Marocco et al. 2019) and CWISEP J1446–2317 (Marocco et al. 2020; Meisner et al. 2020). These three objects constitute a small sample bridging the known Y-dwarf population to WISE J0855–0714 (Luhman 2014). Constraining the initial mass function (IMF) observationally is crucial to understanding the low-mass limit of brown dwarf formation, and Y dwarfs are the lowest-mass piece in the present-day luminosity function that maps onto an IMF. Perhaps the most fundamental open question in brown dwarf science is how these low-mass objects form. Brown dwarfs most likely form in a process similar to an extension of star formation, i.e., from the gravitational collapse of a molecular cloud. However, the mechanisms leading to an initial collapse at lower masses (e.g., turbulent fragmentation; Padoan & Nordlund 2002), to formation

Table 3
HST and Spitzer Photometry

Parameter	WISEA J0014+7951	WISEA J0830+2837	WISEA J0830−6323	WISEA J1516+7217	WISEA J1525+6053
HST Ap. <i>F105W</i> (mag)	20.924 ± 0.015	≥25.4	20.225 ± 0.010	21.470 ± 0.013	21.173 ± 0.013
HST Ap. <i>F125W</i> (mag)	19.993 ± 0.008	≥25.2	19.297 ± 0.004	20.557 ± 0.007	20.233 ± 0.006
HST Ap. <i>F105W</i> − <i>F125W</i> (mag)	0.931 ± 0.017	...	0.928 ± 0.011	0.913 ± 0.015	0.940 ± 0.014
Spitzer PRF <i>ch1</i> (mag)	17.727 ± 0.068	19.089 ± 0.232	17.514 ± 0.058	18.121 ± 0.096	18.000 ± 0.084
Spitzer PRF <i>ch2</i> (mag)	15.880 ± 0.021	15.837 ± 0.021	15.682 ± 0.019	15.946 ± 0.021	15.874 ± 0.021
Spitzer PRF <i>ch1</i> − <i>ch2</i> (mag)	1.847 ± 0.071	3.252 ± 0.233	1.832 ± 0.061	2.175 ± 0.098	2.126 ± 0.087
Spitzer Ap. <i>ch1</i> (mag)	17.777 ± 0.050	19.110 ± 0.166	17.479 ± 0.040	18.220 ± 0.072	18.048 ± 0.063
Spitzer Ap. <i>ch2</i> (mag)	15.845 ± 0.017	15.854 ± 0.018	15.669 ± 0.017	15.947 ± 0.018	15.893 ± 0.018
Spitzer Ap. <i>ch1</i> − <i>ch2</i> (mag)	1.932 ± 0.053	3.256 ± 0.167	1.810 ± 0.043	2.273 ± 0.074	2.155 ± 0.655
Discoverer ^a	1, 2, 3, 4, 5, 7	1, 2	2, 5	2	2, 6

Note.

^a (1) Dan Caselden; (2) Guillaume Colin; (3) Sam Goodman; (4) Austin Rothermich; (5) Nikolaj Stevnbak; (6) Melina Thevenot; (7) Jim Walla.

Table 4

Preliminary WISE and Spitzer Parallax and Motion Fit for WISE 0830+2837

Parameter	Value
R.A. at t_0	127.549578(114.9)
Decl. at t_0	28.617508(74.3)
t_0 (MJD)	57762.10
π_{abs} (mas)	90.6 ± 13.7
$\mu_{\text{R.A.}}$ (mas yr ^{−1})	−233.3 ± 48.6
$\mu_{\text{decl.}}$ (mas yr ^{−1})	−2040.8 ± 29.9
χ^2	20.370
Dof	29
Red. χ^2	0.702

in different locations (e.g., disk fragmentation; Stamatellos & Whitworth 2009), to halt accretion onto a protostar (e.g., photoevaporation or by ejection of prestellar cores; Reipurth & Clarke 2001; Whitworth & Zinnecker 2004, respectively) have not been fully determined.

The minimum fragmentation mass is determined by the opacity of the gas in a molecular cloud, as high densities cause it to become opaque to its own radiation, and leading to a maximum density at which fragmentation can occur (Low & Lynden-Bell 1976; Rees 1976; Silk 1977a, 1977b). From simple critical Jeans mass arguments (Jeans 1902), Low & Lynden-Bell (1976) derived a minimum fragmentation mass of $7 M_{\text{Jup}}$, not taking into account effects from magnetic fields, rotation, or late accretion. Magneto-hydrodynamical simulations from Bate (2012) which include these effects, as well as turbulence, shock compression, and radiative feedback, find a lower minimum fragmentation mass of $3 M_{\text{Jup}}$ (see also Boyd & Whitworth 2005; Padoan et al. 2005, 2007). Observationally, Kirkpatrick et al. (2019) set an initial constraint on the minimum fragmentation mass of $5 M_{\text{Jup}}$ by fitting a simulated population from evolutionary models to their luminosity functions. However, this result is sensitive to the frequency of coldest Y dwarfs, which only included WISE J0855−0714 at the time of publication. WISEA J0830+2837, CWISEP J1446−2317, and CWISEP J1935−1546 are critical additions to the currently undersampled $T_{\text{eff}} \lesssim 300$ K population, and are essential to confidently constrain the low-mass cutoff of the substellar IMF. To see whether the theoretically predicted minimum fragmentation masses do indeed describe the observed brown dwarf population, future empirical studies of the IMF will need to incorporate the growing sample of

“missing link” Y dwarfs. However, such calculations are beyond the scope of this work.

5.2. Characterization of Low-temperature Atmospheres, from the T/Y Dwarf Transition to Jupiter

Our sample contains five ultracool dwarfs, one of which connects the population of known Y dwarfs with the coldest brown dwarf ever discovered. The rest of our targets are most likely late-T dwarfs based on the available evidence. WISEA J0830+2837 is the 29th Y dwarf ever discovered, and the first one from the BYW:P9 collaboration. While most Y dwarfs have been spectroscopically confirmed, their intrinsic faintness in NIR leads to poor S/N and an incomplete characterization of their atmospheric composition. The best atmospheric analog for these extremely cold brown dwarfs is Jupiter itself. While T dwarfs have atmospheres rich in methane and water, identified by the deep absorption bands in their near-infrared spectra, Y dwarfs are expected to have water vapor clouds (Faherty et al. 2014; Skemer et al. 2016; Morley et al. 2018). At the T/Y-dwarf boundary, Na and K alkalis completely disappear (Zalesky et al. 2019), drastically affecting the *Y*−*J* colors at the boundary. At the low temperatures of Y dwarfs, atmospheric models predict the emergence of NH₃ in their NIR spectra (Lodders & Fegley 2002; Burrows et al. 2003; Leggett et al. 2007), and condensation of salt and sulfide clouds (Morley et al. 2012). While tentative ammonia absorption has been observed in the NIR spectrum of an object at the T/Y transition (Burgasser et al. 2012), and NH₃ abundances have been extracted from atmospheric retrievals of Y-dwarf NIR spectra as absorption features were attributed to this gas (Zalesky et al. 2019), a conclusive absorption feature matching theoretical predictions is still lacking (e.g., Schneider et al. 2015). Phosphine, which abounds in the Jovian atmosphere at 4.5–4.6 μm , was also expected in Y dwarfs. However, mid-infrared spectra of WISE J0855−0714 did not show indications of this molecule (Skemer et al. 2016; Morley et al. 2018). Therefore, we need higher S/N, higher resolution spectra, and/or a broader wavelength coverage, as well as more developed line lists for these molecules, to identify the components of low-temperature atmospheres.

Observationally, the spread in colors currently seen at the T/Y-dwarf boundary and throughout the Y-dwarf class, could be driven by metallicity, gravity, binarity, cloud coverage, or variability effects. A predicted reversal of NIR color trend from

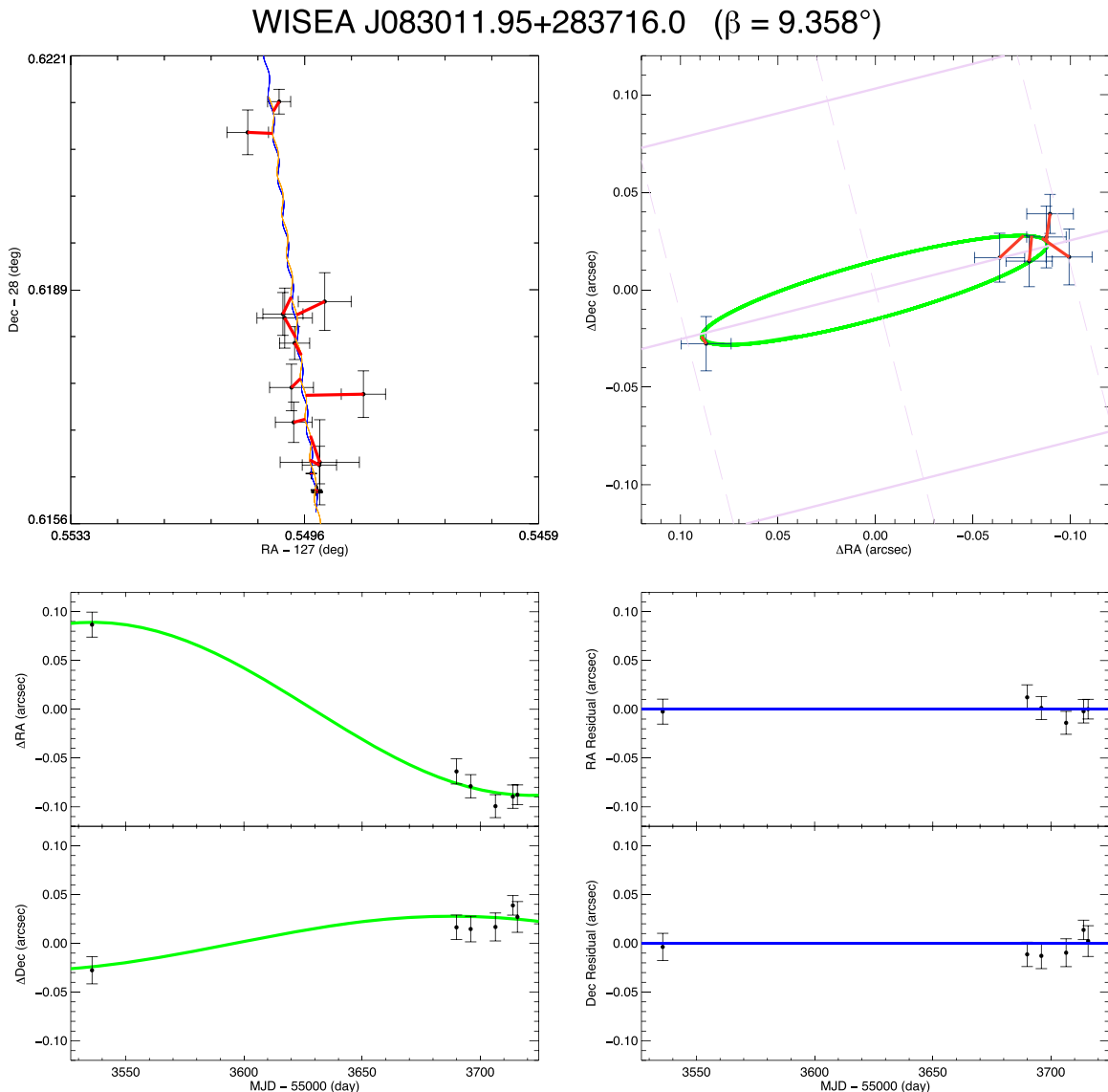


Figure 3. Our fit to the astrometry of WISEA 0830+2837. The full solution and full data sets are shown in the upper left panel, where the unWISE data points are the black points with large error bars and the Spitzer data points are the black points with the much smaller error bars. The blue curve is the expected astrometric path of the object as seen from Spitzer, and the orange curve is the path as seen from the Earth. Each of the observed data points is connected by a red line back to the spot on the relevant curve that has the same time stamp. The other panels—the parallax-only solution (green curve, upper right), residuals around the parallax solution (lower left), and residuals around the full solution (lower right)—show only the Spitzer data points, for clarity.

bluer in T dwarfs to redder in Y dwarfs (Burrows et al. 2003; Saumon et al. 2012; Morley et al. 2014b) has been confirmed with a spectral energy distribution of WISE J0855–0714 (Luhman & Esplin 2016), and attributed to energy redistribution at longer wavelengths at colder temperatures, and the collapse of the Wien tail (Schneider et al. 2016). Faherty et al. (2014) interpreted their J3–[4.5] color measurement as an indication of water ice and sulfide clouds based on equilibrium chemistry models. On the other hand, Luhman & Esplin (2014) were able to reproduce this color with cloudless, disequilibrium chemistry models, leading to the conclusion that no set of models could simultaneously reproduce the near and mid-infrared photometry (Luhman & Esplin 2016; Schneider et al. 2016). However, Skemer et al. (2016) and Morley et al. (2018) disputed the Luhman & Esplin (2014) result and validated water ice clouds as the interpretation for the absorption features in the 3.4–5.2 μm spectra. Finally, photometric variability at a 4% level was detected in WISE J0855–0714 in the

mid-infrared (Esplin et al. 2016), suggesting a patchy atmosphere, yet the cloud composition remains unclear.

WISEA J0830+2837, along with CWISEP J1935–1546 and CWISEP 1446–2317, fill an important gap in the Y-dwarf sequence to continuously map atmospheric composition across low temperatures down to Jupiter. Atmospheric retrievals on a medium-resolution, near-infrared spectrum of this object with NIRSpec aboard the JWST would provide the necessary S/N to identify individual absorption lines and bands to characterize their atmospheres.

6. Conclusions

We have analyzed HST and Spitzer photometry of a sample of five ultracool dwarfs identified through the Backyard Worlds: Planet 9 project. We have identified four late-T dwarfs within 30 pc and one of the coldest Y dwarfs ever recorded, WISEA J0830+2837. This source has a solid detection in *ch1*

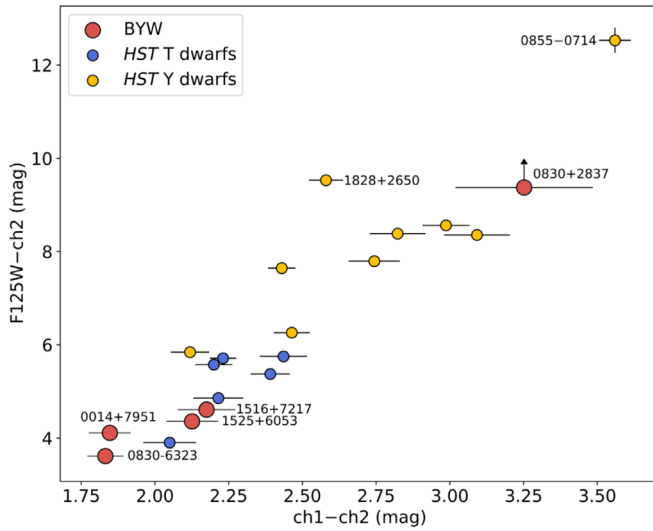


Figure 4. Color-color diagram of Spitzer $ch1-ch2$ color against $F125W-ch2$. Our Backyard Worlds sample is colored in red. HST and Spitzer photometry for T and Y dwarfs from Schneider et al. (2015, 2016) are shown as blue and yellow circles, respectively. The Spitzer photometry of WISEA J0830+2837 places it solidly in the Y-dwarf populated region, with extremely red colors bridging the gap between WISE J0855-0714 and the rest of the Y-dwarf population.

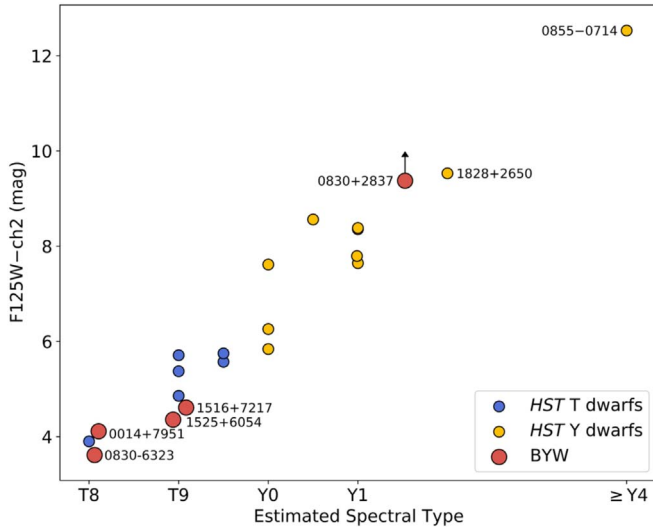


Figure 5. Estimated spectral type vs. HST and Spitzer color. Our Backyard Worlds/Spitzer sample is colored in red. T and Y dwarfs from (Schneider et al. 2016) are shown in blue and yellow, respectively. Error bars for our sample are smaller than the symbol size, on average ~ 0.05 mag.

Table 5

Estimated Physical Properties of Our Sample Based on Spitzer Colors and Parallax Measurement for WISEA J0830+2837

Source	Photometric Type	T_{eff} (K)	Distance (pc)
WISEA J0014+7951	T8	659 ± 85	28 ± 4
WISEA J0830+2837	$\geq Y1$	303 ± 87	9 ± 2
	$\geq Y1^a$	354 ± 73^a	$11.1^{+2.0}_{-1.5}^a$
WISEA J0830-6323	T8	664 ± 84	26 ± 4
WISEA J1516+7217	T9	548 ± 87	24 ± 4
WISEA J1525+6053	T9	563 ± 86	24 ± 4

Note.

^a Calculated distance and estimated photometric type and effective temperature from Spitzer parallax measurement.

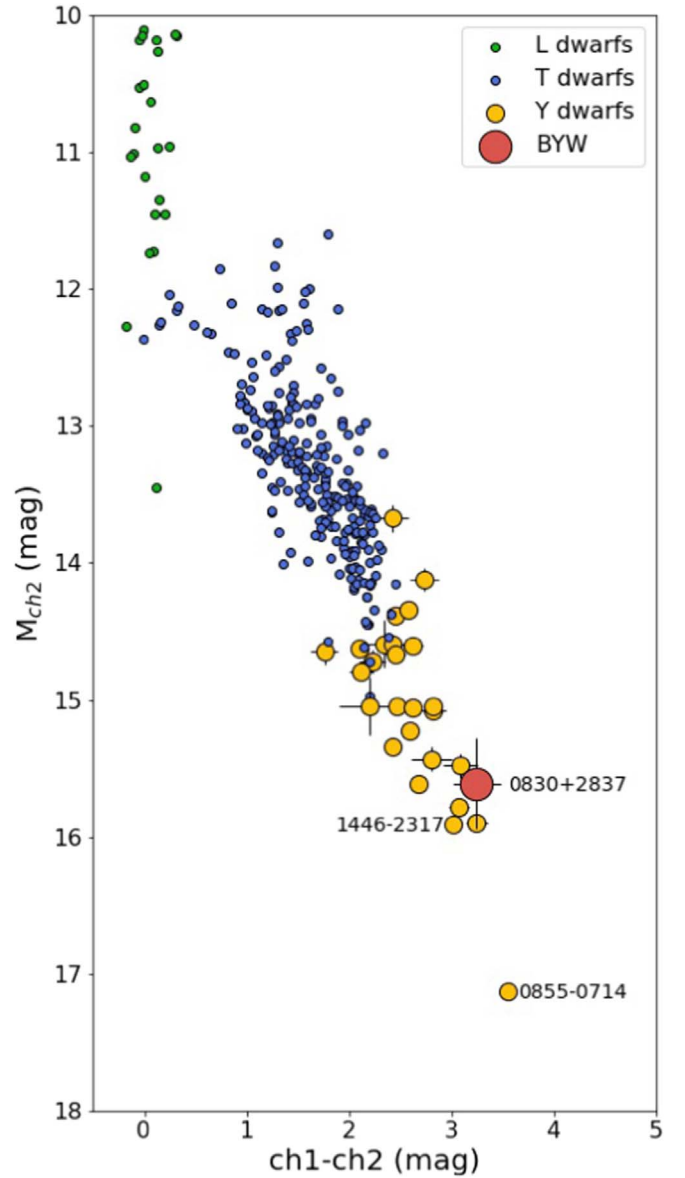


Figure 6. Color-magnitude diagram in Spitzer IRAC $ch2$ -band. L-dwarf parallaxes and $ch2$ photometry come from the Database of Ultracool Parallaxes Dupuy & Liu (2012), Dupuy & Kraus (2013), Liu et al. (2016); T and Y-dwarf parallaxes come from Kirkpatrick et al. (2019). WISEA J0830+2837 joins CWISEP J1935-1546 and CWISEP J1446-2317 in a small, yet growing sample of “missing link” objects bridging the known Y-dwarf population to the coldest brown dwarf known, WISE J0855-0714.

and $ch2$ Spitzer bands, but it drops out on both $F105W$ and $F125W$ HST bands. These HST bands are centered in near-infrared wavelengths, where this cold object no longer emits sufficient flux to be detected, while most of its energy is being emitted in longer, mid-infrared wavelengths to which the Spitzer filters are sensitive. WISEA J0830+2837 joins CWISEP J1935-1546 and CWISEP 1446-2317 in a small sample of objects serving as a bridge between WISE J0855-0714 and the known population of Y dwarfs. The Backyard Worlds: Planet 9 citizen science project is proving its efficacy at identifying the coldest brown dwarfs, and will continue to provide exceptional targets for follow-up observations.

We thank the anonymous referee for their helpful and insightful suggestions that have greatly improved the clarity of

this paper. The “Backyard Worlds: Planet 9” team would like to thank the many Zooniverse volunteers who have participated in this project, from providing feedback during the beta review stage to classifying flipbooks to contributing to the discussions on TALK. We would also like to thank the Zooniverse web development team for their work creating and maintaining the Zooniverse platform and the Project Builder tools. This research was supported by NASA ADAP grant NNH17AE75I. This publication makes use of data products from the Wide-field Infrared Survey Explorer, which is a joint project of the University of California, Los Angeles, and the Jet Propulsion Laboratory/California Institute of Technology, funded by the National Aeronautics and Space Administration. This research has made use of the NASA/IPAC Infrared Science Archive, which is funded by the National Aeronautics and Space Administration and operated by the California Institute of Technology. This research has made use of the Vizier catalog access tool, CDS, Strasbourg, France (DOI:10.26093/cds/vizier). The original description of the Vizier service was published in 2000, *A&A* 143, 23. This research made use of APLpy, an open-source plotting package for Python (Robitaille & Bressert 2012).

Facilities: HST (WFC3), Spitzer (IRAC), IRSA, WISE.


Software: APLpy (Robitaille & Bressert 2012), astrodrizzle (Gonzaga et al. 2012), astropy (Astropy Collaboration et al. 2013), MOPEX/APEX (Makovoz & Marleau 2005), Pandas (McKinney 2013), photutils (Bradley et al. 2019), SAOviewerDS9 (Joye & Mandel 2003), WiseView (Caselden et al. 2018).

ORCID iDs

Daniella C. Bardalez Gagliuffi  <https://orcid.org/0000-0001-8170-7072>

Jacqueline K. Faherty  <https://orcid.org/0000-0001-6251-0573>

Adam C. Schneider  <https://orcid.org/0000-0002-6294-5937>

Aaron Meisner  <https://orcid.org/0000-0002-1125-7384>

Dan Caselden  <https://orcid.org/0000-0001-7896-5791>

Sam Goodman  <https://orcid.org/0000-0003-2236-2320>

J. Davy Kirkpatrick  <https://orcid.org/0000-0003-4269-260X>

Marc Kuchner  <https://orcid.org/0000-0002-2387-5489>

Jonathan Gagné  <https://orcid.org/0000-0002-2592-9612>

Sarah E. Logsdon  <https://orcid.org/0000-0002-9632-9382>


Adam J. Burgasser  <https://orcid.org/0000-0002-6523-9536>

Katelyn Allers  <https://orcid.org/0000-0003-0580-7244>

John Debes  <https://orcid.org/0000-0002-1783-8817>

John Wisniewski  <https://orcid.org/0000-0001-9209-1808>

Austin Rothermich  <https://orcid.org/0000-0003-4083-9962>

Nikolaj Stevnbak Andersen  <https://orcid.org/0000-0003-4714-3829>

Melina Thévenot  <https://orcid.org/0000-0001-5284-9231>

References

Astropy Collaboration, Robitaille, T. P., Tollerud, E. J., et al. 2013, *A&A*, 558, A33

Baraffe, I., Homeier, D., Allard, F., & Chabrier, G. 2015, *A&A*, 577, A42

Bate, M. R. 2012, *MNRAS*, 419, 3115

Boffin, H. M. J., Pourbaix, D., Mužić, K., et al. 2014, *A&A*, 561, L4

Boyd, D. F. A., & Whitworth, A. P. 2005, *A&A*, 430, 1059

Bradley, L., Sipocz, B., Robitaille, T., et al. 2019, *astropy/photutils*: v0.7, Zenodo, doi:10.5281/zenodo.3368647

Burgasser, A. J. 2004, *ApJS*, 155, 191,

Burgasser, A. J., Gelino, C. R., Cushing, M. C., & Kirkpatrick, J. D. 2012, *ApJ*, 745, 26,

Burgasser, A. J., Gillon, M., Melis, C., et al. 2015, *AJ*, 149, 104,

Burrows, A., Sudarsky, D., & Lunine, J. I. 2003, *ApJ*, 596, 587,

Caselden, D., Westin, P. I., Meisner, A., Kuchner, M., & Colin, G. 2018, WiseView: Visualizing Motion and Variability of Faint WISE Sources, Astrophysics Source Code Library, ascl:1806.004

Cushing, M. C., Kirkpatrick, J. D., Gelino, C. R., et al. 2011, *ApJ*, 743, 50

Debes, J. H., Thévenot, M., Kuchner, M. J., et al. 2019, *ApJL*, 872, L25

Dupuy, T. J., & Kraus, A. L. 2013, *Sci*, 341, 1492

Dupuy, T. J., & Liu, M. C. 2012, *ApJS*, 201, 19

Dupuy, T. J., Liu, M. C., Best, W. M. J., et al. 2019, *AJ*, 158, 174

Dupuy, T. J., Liu, M. C., & Leggett, S. K. 2015, *ApJ*, 803, 102

Dye, S., Lawrence, A., Read, M. A., et al. 2018, *MNRAS*, 473, 5113

Eisenhardt, P. R. M., Marocco, F., Fowler, J. W., et al. 2020, *ApJS*, 247, 69

Esplin, T. L., Luhman, K. L., Cushing, M. C., et al. 2016, *ApJ*, 832, 58

Faherty, J. K., Burgasser, A. J., Cruz, K. L., et al. 2009, *AJ*, 137, 1

Faherty, J. K., Burgasser, A. J., Walter, F. M., et al. 2012, *ApJ*, 752, 56

Faherty, J. K., Goodman, S., Caselden, D., et al. 2020, *ApJ*, 889, 176

Faherty, J. K., Tinney, C. G., Skemer, A., & Monson, A. J. 2014, *ApJL*, 793, L16

Gennaro, M., Anderson, J., Baggett, S., et al. 2018, WFC3 Data Handbook, Version 4.0 (Baltimore, MD: STScI), <https://hst-docs.stsci.edu/wfc3dhh>

Gonzaga, S., Hack, W., Fruchter, A., & Mack, J. 2012, The DrizzlePac Handbook (Baltimore, MD: STScI), https://www.stsci.edu/files/live/sites/www/files/home/scientific-community/software/drizzlepac/_documents/drizzlepac-handbook.pdf

Hanel, R., Conrath, B., Herath, L., Kunde, V., & Pirraglia, J. 1981, *JGR*, 86, 8705

Jeans, J. H. 1902, *RSPTA*, 199, 1

Joye, W. A., & Mandel, E. 2003, in ASP Conf. Ser. 295, New Features of SAOImage DS9, ed. H. E. Payne, R. I. Jedrzejewski, & R. N. Hook (San Francisco, CA: ASP), 489

Kirkpatrick, J. D., Cushing, M. C., Gelino, C. R., et al. 2013, *ApJ*, 776, 128

Kirkpatrick, J. D., Gelino, C. R., Cushing, M. C., et al. 2012, *ApJ*, 753, 156

Kirkpatrick, J. D., Kellogg, K., Schneider, A. C., et al. 2016, *ApJS*, 224, 36

Kirkpatrick, J. D., Martin, E. C., Smart, R. L., et al. 2019, *ApJS*, 240, 19

Kuchner, M. J., Faherty, J. K., Schneider, A. C., et al. 2017, *ApJL*, 841, L19

Lang, D. 2014, *AJ*, 147, 108

Leggett, S. K., Marley, M. S., Freedman, R., et al. 2007, *ApJ*, 667, 537

Liu, M. C., Dupuy, T. J., & Allers, K. N. 2016, *ApJ*, 833, 96

Liu, M. C., Dupuy, T. J., Bowler, B. P., Leggett, S. K., & Best, W. M. J. 2012, *ApJ*, 758, 57

Lodders, K., & Fegley, B. 2002, *Icar*, 155, 393

Low, C., & Lynden-Bell, D. 1976, *MNRAS*, 176, 367

Luhman, K. L. 2014, *ApJL*, 786, L18

Luhman, K. L., Burgasser, A. J., & Bochanski, J. J. 2011, *ApJL*, 730, L9

Luhman, K. L., & Esplin, T. L. 2014, *ApJ*, 796, 6

Luhman, K. L., & Esplin, T. L. 2016, *AJ*, 152, 78

Luyten, W. J. 1922, *LicOB*, 336, 135

MacKenty, J. W., Kimble, R. A., O’Connell, R. W., & Townsend, J. A. 2008, *Proc. SPIE*, 7010, 70101F

Mainzer, A., Bauer, J., Cutri, R. M., et al. 2014, *ApJ*, 792, 30

Mainzer, A., Grav, T., Bauer, J., et al. 2011, *ApJ*, 743, 156

Makovoz, D., & Marleau, F. R. 2005, *PASP*, 117, 1113

Mamajek, E. E., Barenfeld, S. A., Ivanov, V. D., et al. 2015, *ApJL*, 800, L17

Marocco, F., Caselden, D., Meisner, A. M., et al. 2019, *ApJ*, 881, 17

Marocco, F., Kirkpatrick, J. D., Meisner, A. M., et al. 2020, *ApJL*, 888, L19

Martin, E. C., Kirkpatrick, J. D., Beichman, C. A., et al. 2018, *ApJ*, 867, 109

McKinney, W. 2013, Python for Data Analysis: Data Wrangling with Pandas, NumPy, and IPython (1st ed.; Beijing: O’Reilly)

McMahon, R. G., Banerji, M., Gonzalez, E., et al. 2013, *Msngr*, 154, 35

Meisner, A. M., Caselden, D., Kirkpatrick, J. D., et al. 2020, *ApJ*, 889, 74

Meisner, A. M., Lang, D., & Schlegel, D. J. 2017a, *AJ*, 154, 161

Meisner, A. M., Lang, D., & Schlegel, D. J. 2017b, *AJ*, 153, 38

Meisner, A. M., Lang, D., & Schlegel, D. J. 2018a, *AJ*, 156, 69

Meisner, A. M., Lang, D. A., & Schlegel, D. J. 2018b, *RNAAS*, 2, 202

Morley, C. V., Fortney, J. J., Marley, M. S., et al. 2012, *ApJ*, 756, 172

Morley, C. V., Marley, M. S., Fortney, J. J., et al. 2014a, *ApJ*, 787, 78

Morley, C. V., Marley, M. S., Fortney, J. J., & Lupu, R. 2014b, *ApJL*, 789, L14

Morley, C. V., Skemer, A. J., Allers, K. N., et al. 2018, *ApJ*, 858, 97

Morley, C. V., Skemer, A. J., Miles, B. E., et al. 2019, *ApJL*, 882, L29

Padoan, P., & Nordlund, Å. 2002, *ApJ*, 576, 870

Padoan, P., Kritsuk, A., Michael, N. L., & Nordlund, Å. 2005, *MmSAI*, 76, 187

- Padoan, P., Nordlund, Å., Kritsuk, A. G., Norman, M. L., & Li, P. S. 2007, *ApJ*, 661, 972
- Pinfield, D. J., Gromadzki, M., Leggett, S. K., et al. 2014, *MNRAS*, 444, 1931
- Rees, M. J. 1976, *MNRAS*, 176, 483
- Reipurth, B., & Clarke, C. 2001, *AJ*, 122, 432
- Robitaille, T., & Bressert, E. 2012, APLpy: Astronomical Plotting Library in Python, Astrophysics Source Code Library, ascl:1208.017
- Saumon, D., Marley, M. S., Abel, M., Frommhold, L., & Freedman, R. S. 2012, *ApJ*, 750, 74
- Schneider, A., Burgasser, A., Gerasimov, R., et al. 2020, *ApJ*, submitted
- Schneider, A. C., Cushing, M. C., Kirkpatrick, J. D., et al. 2015, *ApJ*, 804, 92
- Schneider, A. C., Cushing, M. C., Kirkpatrick, J. D., & Gelino, C. R. 2016, *ApJL*, 823, L35
- Scholz, R.-D. 2014, *A&A*, 561, A113
- Silk, J. 1977a, *ApJ*, 214, 152
- Silk, J. 1977b, *ApJ*, 214, 718
- Skemer, A. J., Morley, C. V., Allers, K. N., et al. 2016, *ApJL*, 826, L17
- Skrutskie, M. F., Cutri, R. M., Stiening, R., et al. 2006, *AJ*, 131, 1163
- Stamatellos, D., & Whitworth, A. P. 2009, *MNRAS*, 392, 413
- Stetson, P. B. 1987, *PASP*, 99, 191
- Tinney, C. G., Faherty, J. K., Kirkpatrick, J. D., et al. 2012, *ApJ*, 759, 60
- Tinney, C. G., Faherty, J. K., Kirkpatrick, J. D., et al. 2014, *ApJ*, 796, 39
- Tinney, C. G., Kirkpatrick, J. D., Faherty, J. K., et al. 2018, *ApJS*, 236, 28
- Visscher, C., Lodders, K., & Fegley, B. J. 2006, *ApJ*, 648, 1181
- Whitworth, A. P., & Zinnecker, H. 2004, *A&A*, 427, 299
- Wright, E. L., Eisenhardt, P. R. M., Mainzer, A. K., et al. 2010, *AJ*, 140, 1868
- Zalesky, J. A., Line, M. R., Schneider, A. C., & Patience, J. 2019, *ApJ*, 877, 24